

RESEARCH ARTICLE



Sensitive detection of SARS-CoV-2 main protease 3CL^{pro} with an engineered ribonuclease zymogen

Evans C. Wralstad | Ronald T. Raines

Department of Chemistry, Massachusetts Institute of Technology, Cambridge, Massachusetts, USA

Correspondence

Ronald T. Raines, Department of Chemistry, Massachusetts Institute of Technology, 77 Massachusetts Avenue, Room 18-498, Cambridge, MA 02139-4307, USA.
Email: rtraines@mit.edu

Funding information

National Institutes of Health, Grant/Award Numbers: R01 CA073808, R21 AI171663

Review Editor: Aitziber L. Cortajarena

Abstract

Alongside vaccines and antiviral therapeutics, diagnostic tools are a crucial aid in combating the COVID-19 pandemic caused by the etiological agent SARS-CoV-2. All common assays for infection rely on the detection of viral sub-components, including structural proteins of the virion or fragments of the viral genome. Selective pressure imposed by human intervention of COVID-19 can, however, induce viral mutations that decrease the sensitivity of diagnostic assays based on biomolecular structure, leading to an increase in false-negative results. In comparison, mutations are unlikely to alter the *function* of viral proteins, and viral machinery is under less selective pressure from vaccines and therapeutics. Accordingly, diagnostic assays that rely on biomolecular function can be more robust than ones that rely on biopolymer structure. Toward this end, we used a split intein to create a circular ribonuclease zymogen that is activated by the SARS-CoV-2 main protease, 3CL^{pro}. Zymogen activation by 3CL^{pro} leads to a >300-fold increase in ribonucleolytic activity, which can be detected with a highly sensitive fluorogenic substrate. This coupled assay can detect low nanomolar concentrations of 3CL^{pro} within a timeframe comparable to that of common antigen-detection protocols. More generally, the concept of detecting a protease by activating a ribonuclease could be the basis of diagnostic tools for other indications.

KEYWORDS

circular protein, COVID-19, function-based diagnostic, protease, rapid antigen detection testing, ribonuclease, SARS-CoV-2, zymogen

1 | INTRODUCTION

The COVID-19 pandemic caused by the betacoronavirus SARS-CoV-2 has been a public health crisis of extraordinary proportions. Success in combatting SARS-CoV-2 has been achieved by the development of preventive vaccines, therapeutic interventions, and diagnostic tools (Yuan et al., 2023). Still, the landscape has shifted continually. Several chemotherapeutic agents employed in the treatment of COVID-19, including the neutralizing monoclonal antibodies produced by Lilly, Regeneron,

GlaxoSmithKline, and others, the adenosine nucleoside analog Remdesivir, and the combination protease inhibitor formulation Paxlovid, have exhibited reduced efficacy as a consequence of mutations in the SARS-CoV-2 genome (Gandhi et al., 2022; Planas et al., 2022; Rockett et al., 2022; Service, 2022). Similarly, rapid antigen detection testing (RADT), which often targets the SARS-CoV-2 spike and nucleocapsid proteins and serves as an indispensable front-line tool to mitigate viral transmission, has suffered from reduced sensitivity (de Michelena et al., 2022; Mahmoudinobar et al., 2021). For example,

the appearance of the Omicron SARS-CoV-2 variant led to a days-long lag between the detection of viral infection by RADT versus PCR (Adamson et al., 2022). Even PCR-based testing, which is the gold standard, has lost sensitivity due to “gene dropout” in the spike and nucleocapsid proteins (Ippoliti et al., 2022; Isabel et al., 2022; Robles-Escajeda et al., 2023).

RADT, PCR, and other diagnostic tools rely on the structure of a viral molecule. We sought to develop a diagnostic strategy that relies instead on molecular *function*. Such a function-based approach would mitigate the risk of mutation-based sensitivity loss because viral evolution to evade detection is likely to impair its replisome.

An obvious basis for a diagnostic assay relying on function is the catalytic cleavage of a fluorogenic substrate by a viral enzyme (Chyan & Raines, 2018; Singh et al., 2019; Wu et al., 2022). Such an assay is likely, however, to lack sensitivity because each turnover yields only one fluorescent molecule. We reasoned that the sensitivity could be amplified if the viral enzyme instead activated a zymogen that then catalyzed the cleavage of a fluorogenic substrate (Figure 1). Moreover, we suspected that using two different types of enzymes (e.g., a protease and a nuclease) would avoid complications from crosstalk between the enzymes and their substrates and products.

As a viral analyte, we choose the main protease 3CL^{Pro}. SARS-CoV-2 relies on this protease to process its two polyproteins at 11 cleavage sites, each flanked by a glutamine (P1 = Gln in the Schechter–Berger nomenclature) and a small, uncharged amino acid (P1' = Gly, Ala, or Ser) (Grum-Tokars et al., 2008; Ramos-Guzmán et al., 2020). Recently, we showed that 3CL^{Pro} cleaves the consensus substrate sequence ATLQ↓SGNA (↓, cleavage site) with a high value of $k_{cat}/K_M = (4.3 \pm 0.7) \times 10^4 \text{ M}^{-1} \text{ s}^{-1}$ (Wralstad et al., 2023).

As a zymogen, we choose one engineered from human ribonuclease 1 (RNase 1). The N and C termini of RNase 1 and its homologues flank its active site. Accordingly, connecting the native termini with a peptidic linker occludes the active site (Johnson et al., 2006; Plankum et al., 2003; Turcotte & Raines, 2008; Windsor et al., 2019). The linker of our zymogen contains the sequence: ATLQSGNA, as its cleavage by 3CL^{Pro} would uncover the active site. Zymogen activation could be detected with a hypersensitive assay that is based on a fluorogenic ribonuclease substrate (Kelemen et al., 1999; Park et al., 2001).

Here, we design and prepare a cyclic ribonuclease zymogen, and we demonstrate its specific cleavage by 3CL^{Pro} within its inactivating linker. Specifically, we flank an RNase 1 variant with the *NpuN* and *NpuC* split intein fragments and rely on spontaneous

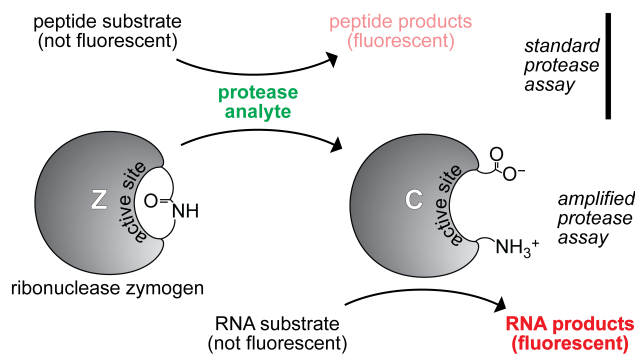


FIGURE 1 Standard and amplified assays for a protease analyte. In a standard assay, a protease cleaves a fluorogenic substrate. In an amplified assay (as in this work), a protease cleaves a peptide bond in the linker of a ribonuclease zymogen (Z), producing a cleaved zymogen (C) with an uncovered active site. Zymogen cleavage is detected by assaying ribonucleolytic activity with a fluorogenic substrate.

posttranslational intein splicing to excise the fragments and ligate the termini, thereby cyclizing the protein and forming the zymogen (Shah & Muir, 2014; Windsor et al., 2019). By monitoring the ensuing ribonucleolytic activity upon zymogen linker cleavage by 3CL^{Pro}, we can detect low nanomolar concentrations of 3CL^{Pro} within a time frame comparable to current RADT. The detection of 3CL^{Pro} at higher concentrations occurs more quickly. Our strategy could inspire next-generation diagnostics that mitigate the sensitivity losses that can result from viral evolution.

2 | RESULTS

2.1 | Modeling the zymogen and its interaction with 3CL^{Pro}

We predicted the structure of our 3CL^{Pro}-directed, RNase 1-based zymogen with the AlphaFold2-based algorithm ColabFold and *in silico* permutations of the zymogen sequence. We designed those permutations to accommodate ColabFold by installing false termini (Mirdita et al., 2022). We assessed the predictions based on their structural similarity to native RNase 1 as well as the proximity of their false termini; four permuted sequences generated sensible zymogen models and are shown in Figure 2a. The permuted sequences, individual model structures, and AlphaFold2 quality metrics are shown in Figure S1. The backbone alignment of the models to wild-type RNase 1 reveals a high degree of structural identity with RMSD $\leq 2.5 \text{ \AA}$. The permutant-dependent false termini are 4.1–20.4 \AA apart (C-terminal carbonyl carbon to N-terminal amino nitrogen). The

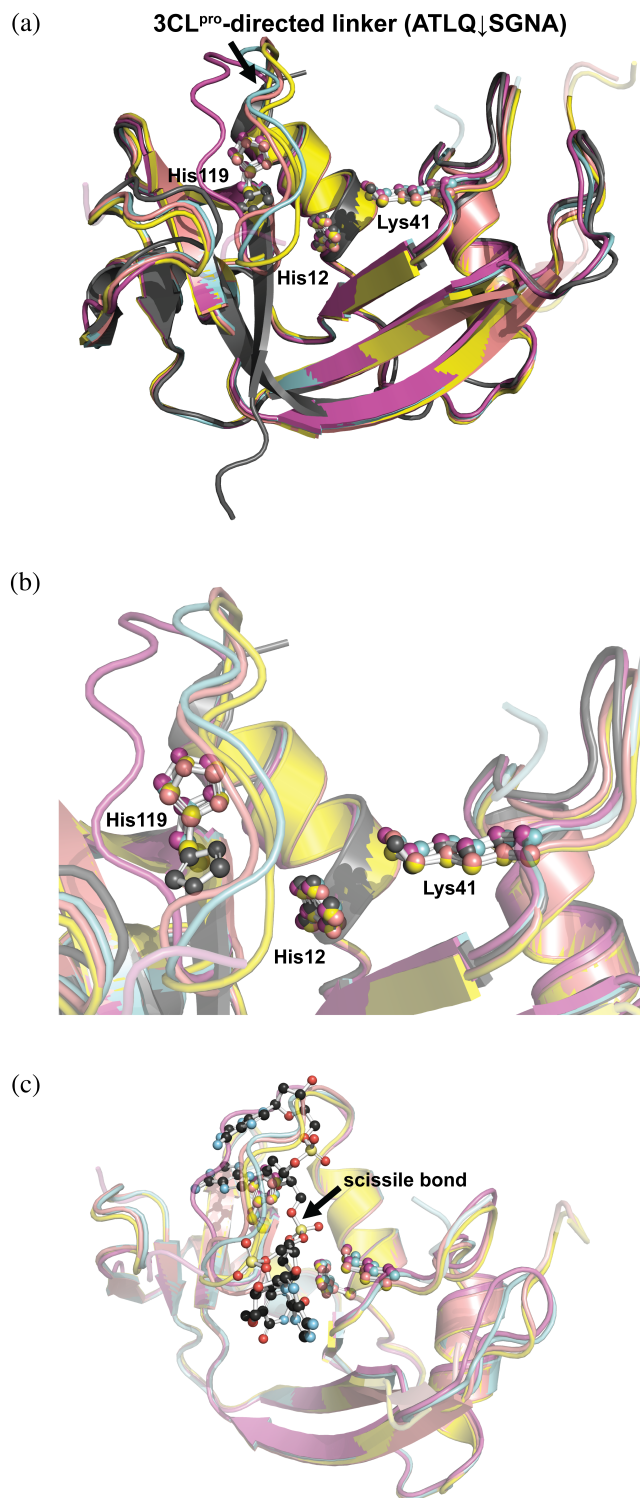


FIGURE 2 AlphaFold2-generated zymogen models. (a) Q37|R38, G68|Q69, N88|R89, and R89|R90 permuted models (in color) aligned to wild-type RNase 1 (in gray), cartoon form with active site residues in ball-and-stick form. (b) Active sites of the zymogen models compared to that of wild-type RNase 1. (c) Docking of the ribonuclease substrate analog dAdT(dA)₂ with the zymogen models. Substrate is in ball-and-stick form/CPK color scheme and is derived from PDB ID 1rcn.

Q37|R38-permuted sequence yielded the shortest terminal distance and was thus a model most reminiscent of the circular zymogen, which has a peptide bond between the false termini.

Catalysis of RNA cleavage by RNase 1 and its homologues relies primarily on the side chains of three residues: His 12, Lys41, and His119 (Figure S2) (Raines, 1998). Based on the AlphaFold2-generated models, we predict that His12 and Lys41 are not significantly perturbed in the zymogen relative to RNase 1, but His119 is dislocated (Figure 2b). This dislocation consistently appears between models: across four permuted zymogen sequences and five ranked models per sequence, the imidazole ring of His119 is rotated $123 \pm 2^\circ$ (mean \pm SD) out of alignment from its native position (Figure 3). Docking the tetranucleotide substrate analog d(ATAA) to the zymogen also reveals a significant steric clash between the zymogen linker and nucleotides on the 3' side of the scissile phosphodiester bond (Figure 2c). We predict that active-site distortion and steric hindrance can work in tandem to diminish the catalytic activity of our engineered zymogen, as occurs in natural zymogens (Khan & James, 1998).

To model interactions between the zymogen and 3CL^{PRO}, we submitted the optimal zymogen model (Q37|R38: 1.08-Å RMSD to RNase 1, 4.8-Å terminal gap) and the structure of SARS-CoV 3CL^{PRO} to the ClusPro protein-protein docking server (Kozakov et al., 2017). We decided to use the 3CL^{PRO} homologue structure in lieu of a structure from SARS-CoV-2 because the former captures the physiologically relevant protease dimer within the crystallographic asymmetric unit rather than generating a dimer by symmetry operations; the two active sites of dimeric 3CL^{PRO} are reported to be conformationally nonidentical, and an accurate representation of the two component protomers is necessary for relevant zymogen docking (Chen et al., 2006; Durdagi et al., 2021; Yang et al., 2003). Because SARS-CoV and SARS-CoV-2 3CL^{PRO} share 96% sequence identity, our docking results are likely to be valid for SARS-CoV-2 3CL^{PRO}.

Surface modeling with ClusPro revealed significant topological complementarity between the zymogen and 3CL^{PRO} (Video S1). Specifically, ClusPro yields a high-ranking model (3 of 30) in which the zymogen linker is inserted into one of the 3CL^{PRO} active sites (Figure 4a). In the zymogen linker, the main-chain C of Gln_Z is the intended electrophile. In the high-ranking model, C of Gln_Z is within 7 Å of S^γ of Cys145, which is the active-site nucleophile (Figure 4b). Notably, 6 of 30 ClusPro docked structures have the scissile bond of the zymogen near the active site of 3CL^{PRO}, with an average S^γ...C distance of 12.3 Å and a range of 7.0–18.5 Å (Figure S3).

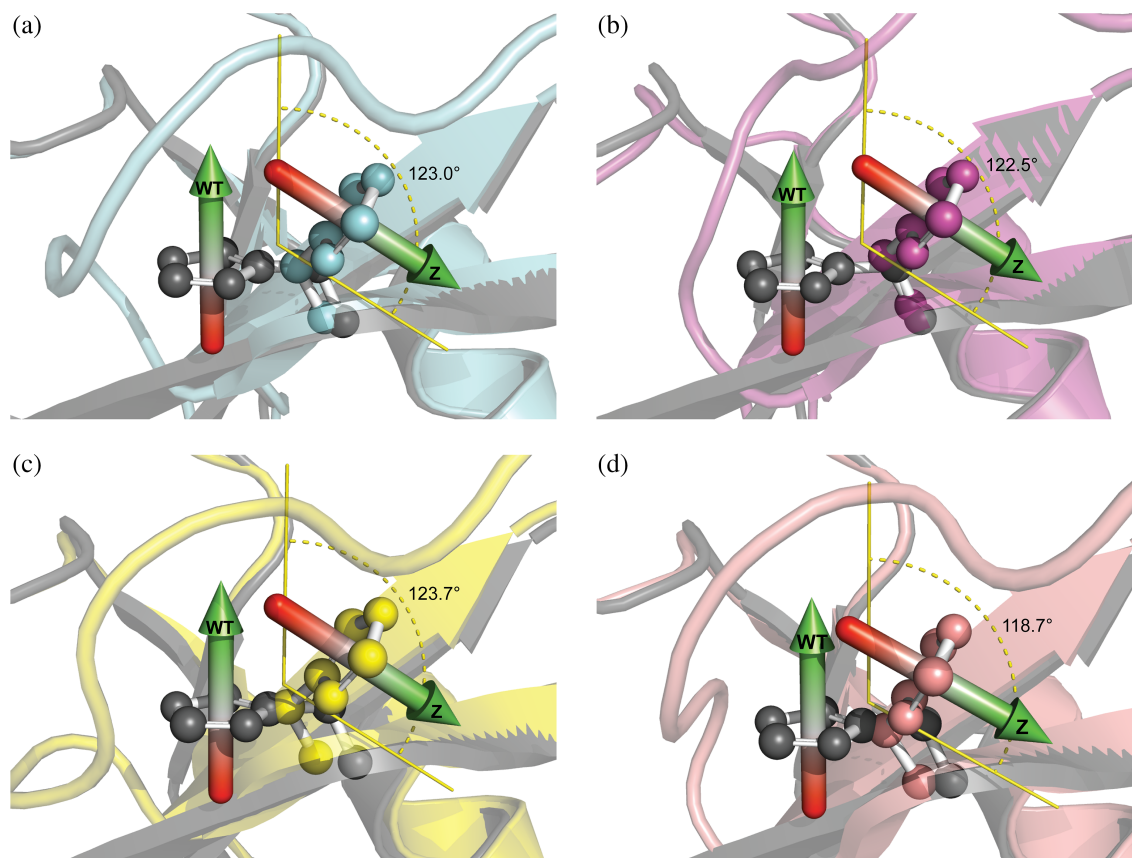


FIGURE 3 Dislocation angle of His119 in the AlphaFold2-generated zymogen structure predictions relative to wild-type RNase 1. Arrows represent the vector normal to the plane of the His119 imidazole ring in the wild-type protein (WT) and in the zymogen (Z). Panels represent the top-ranked model prediction generated with protein sequences circularly permuted around (a) Q37|R38, (b) G68|Q69, (c) N88|R89, and (d) R89|R90.

2.2 | Characterizing the nature of zymogen cleavage by 3CL^{PRO}

We used mass spectrometry to observe zymogen cleavage by 3CL^{PRO} because of the characteristic +18 Da shift upon amide bond hydrolysis. The waterfall plot in Figure 5a shows that over 50% of the zymogen is cleaved within 5 min and that cleavage is virtually complete within 1 h. Heat denaturation experiments revealed that the zymogen is considerably more thermostable upon linker cleavage ($\Delta T_m = 21.0 \pm 0.1^\circ\text{C}$) (Figure 5b), as expected from the release of the conformational strain incurred by cyclization (Windsor et al., 2019). The zymogen also appears to be resistant to off-target proteolysis by 3CL^{PRO}; even after incubating the zymogen with 3CL^{PRO} for 3 h, proteolytic degradation products are not visible by SDS-PAGE (Figure 5c), and mass spectrometry reveals only the +18 Da adduct corresponding to one proteolytic event. Using the tetranucleotide 6-FAM-dArU(dA)₂-6-TAMRA as a fluorogenic ribonuclease substrate, we determined that the uncleaved zymogen has a k_{cat}/K_M value of $(9.0 \pm 0.1) \times 10^3 \text{ M}^{-1} \text{ s}^{-1}$, which is 0.04% that of wild-type

RNase 1. Meanwhile, the fully cleaved zymogen has a k_{cat}/K_M value of $(2.9 \pm 0.1) \times 10^6 \text{ M}^{-1} \text{ s}^{-1}$; thus, the release of cyclic strain restores activity to 14% that of the wild-type enzyme and leads to a 321-fold increase in activity relative to the cyclized protein.

2.3 | Detecting 3CL^{PRO} by the signal amplification of zymogen activation

After demonstrating that the zymogen is cleaved specifically in its linker, we characterized whether the zymogen can be used to detect 3CL^{PRO} and distinguish samples harboring low levels of protease from samples that are protease-free. As expected, ribonucleolytic activity is not observed in the 15-min observation period at any of the employed zymogen concentrations if 3CL^{PRO} is not present (Figure 6). With as little as 50 pM zymogen, we can detect the presence of $\geq 10 \text{ nM}$ 3CL^{PRO} by its activation of the zymogen and the subsequent turnover of our ribonuclease substrate (Figure 6a) (the method for evaluating whether 3CL^{PRO} was detected with statistical significance

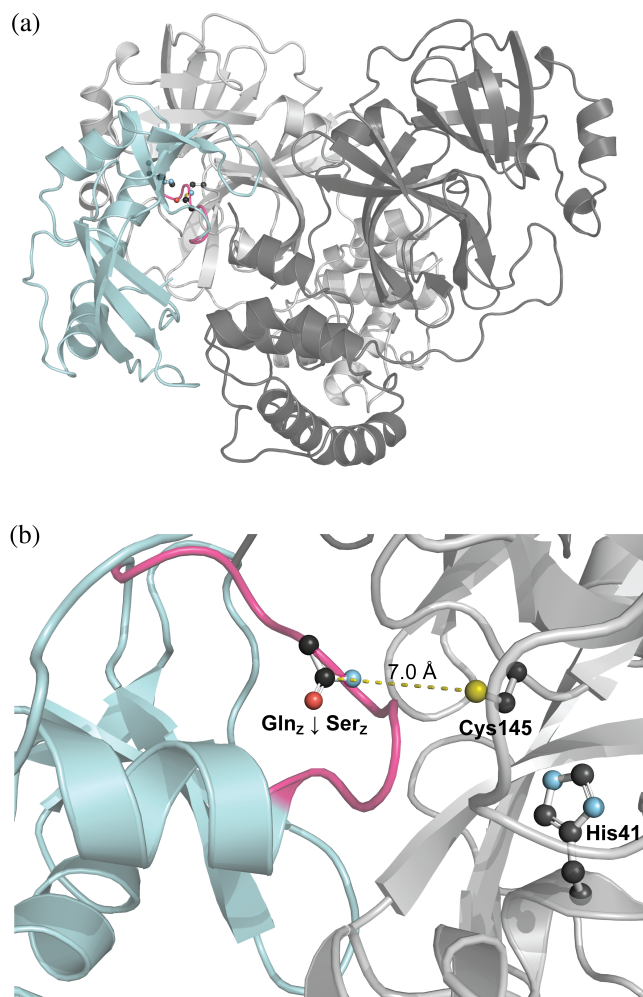


FIGURE 4 ClusPro model of the zymogen interacting with 3CL^{pro}. (a) Interaction of the 3CL^{pro} protomers (cartoon, distinct shades of gray) and the zymogen (cartoon, teal with linker in magenta) with atoms relevant to linker cleavage in ball-and-stick form (CPK color scheme). (b) Location of the scissile amide bond of the zymogen linker (Gln_z ↓ Ser_z) in relation to the 3CL^{pro} catalytic residue Cys145.

is described in Section 4). Increasing the zymogen concentration to 500 pM increases the detection sensitivity to ≥ 5 nM 3CL^{pro} (Figure 6b). The twofold increase in 3CL^{pro} detection sensitivity with a tenfold increase in zymogen concentration suggests that the intrinsic proteolytic activity of 3CL^{pro} on the zymogen linker, rather than the rate of substrate turnover by activated zymogen, limits detection. A further increase in zymogen concentration to 5 nM enabled expeditious detection of 3CL^{pro}. At protease concentrations ≥ 250 nM, over half of the ribonuclease substrate was turned over within the observation period, with quantitative turnover of the substrate achieved at the two highest 3CL^{pro} concentrations (Figure 6c; note the plateau in fluorescence intensity).

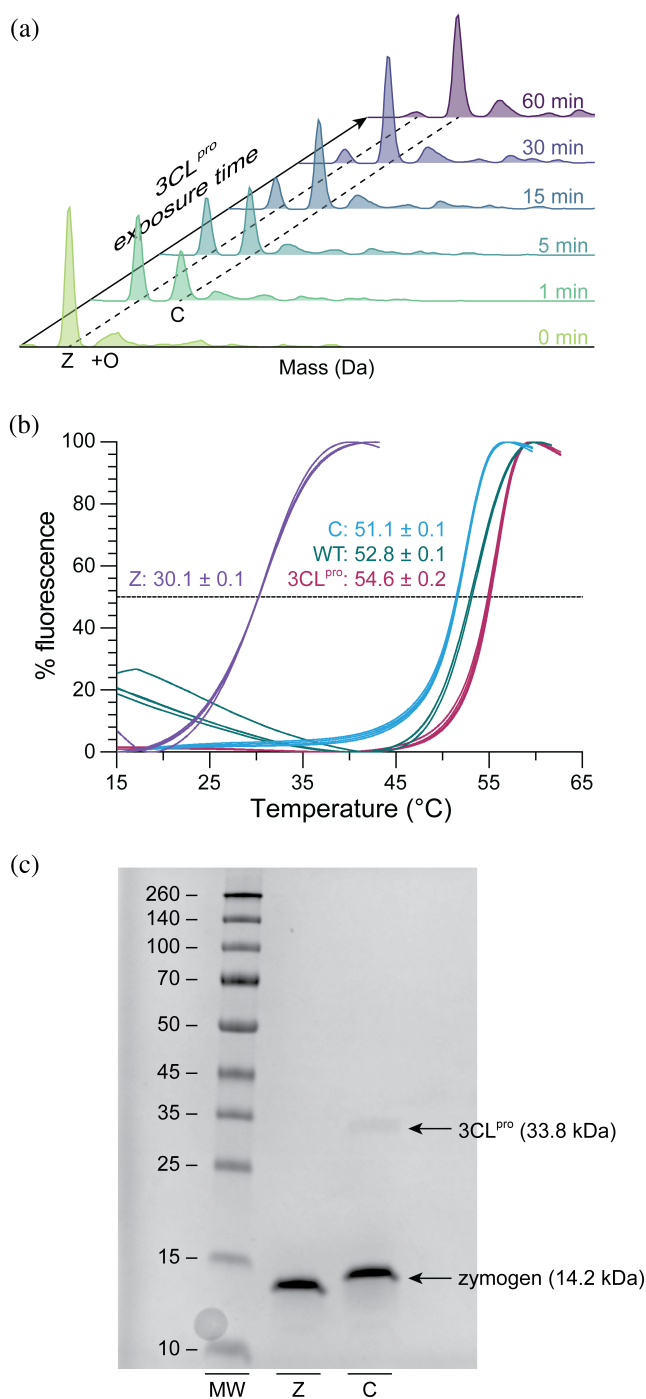


FIGURE 5 Conversion of the zymogen (Z) to cleaved zymogen (C) by 3CL^{pro}. (a) Waterfall plot of deconvoluted mass spectrometry data for zymogen treatment with 3CL^{pro}; peak area is proportional to the percent of total species. +O indicates a +16 Da peak frequently seen in RNase 1 samples due to methionine oxidation. (b) Thermal denaturation curves ($n = 4$ per sample) with wild-type RNase 1 (WT) are shown for comparison. (c) SDS-PAGE of the zymogen before and after 3CL^{pro} treatment for 3 h. MW, molecular weight standards (masses in kDa).

Indeed, over half of the ribonuclease substrate was turned over within 5 min at 1.0 μ M 3CL^{pro} (Figure 6c). All time-course data are shown in Figure S4.

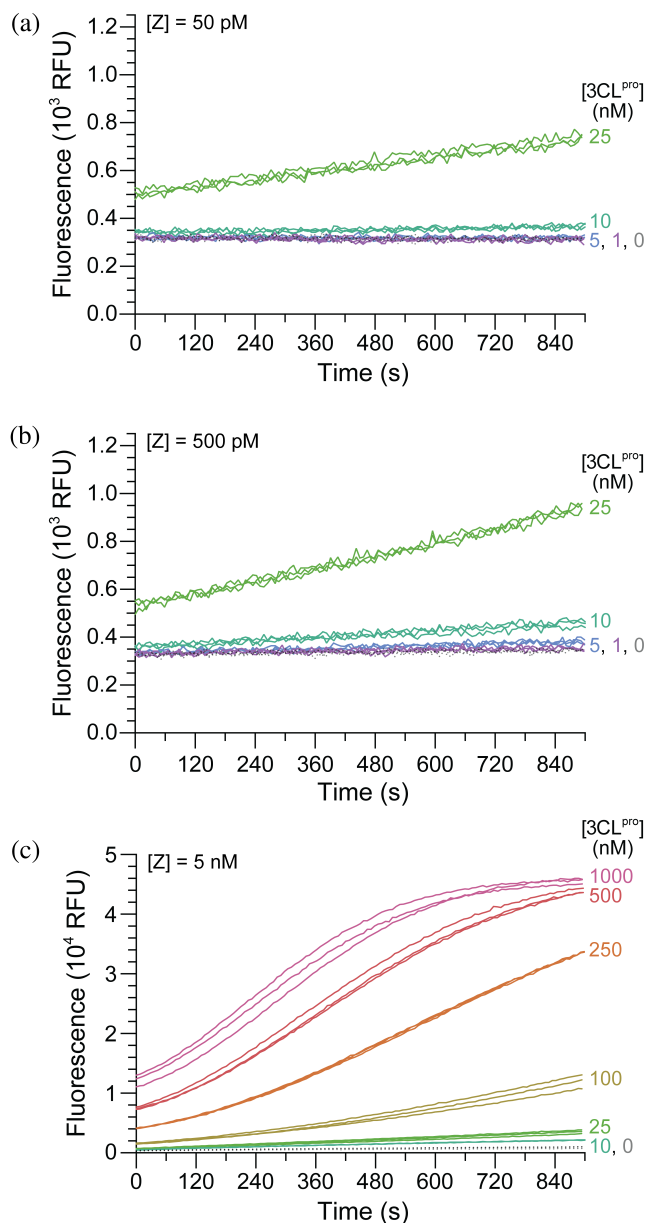


FIGURE 6 Detection of 3CL^{Pro} by zymogen activation with the coupled enzyme activity assay. Fluorescence intensity is shown for turnover of the RNA substrate upon 3CL^{Pro}-mediated cleavage of (a) 50 pM, (b) 500 pM, and (c) 5 nM zymogen. 3CL^{Pro} concentration ($n = 3$ replicates) is indicated by line color.

Using the time-course data for 500 pM and 5 nM zymogen at $[3\text{CL}^{\text{Pro}}] \geq 100$ nM, we modeled the rate of substrate turnover in our coupled reaction detection system and determined that the $k_{\text{cat}}/K_{\text{M}}$ value for the cleavage of the zymogen linker by 3CL^{Pro} was $(1.2 \pm 0.1) \times 10^3 \text{ M}^{-1} \text{ s}^{-1}$ (mean \pm SE). (See Supporting Information for a complete derivation of the equations governing the reaction kinetics and Figure S5 for fits to the time-course data.) For comparison, we recently reported that the same protease substrate sequence installed in the fluorogenic

dodecapeptide R-E(EDANS)-ATLQSGNA-K(DABCYL)-R is cleaved by 3CL^{Pro} with a $k_{\text{cat}}/K_{\text{M}}$ value of $(4.3 \pm 0.7) \times 10^4 \text{ M}^{-1} \text{ s}^{-1}$ (Wralstad et al., 2023).

3 | DISCUSSION

Our zymogen design follows a strategy that we used previously to generate ribonuclease zymogens activated by other viral proteases: terminal truncation of RNase 1 in conjunction with protein cyclization with a peptidic linker to induce conformational strain and steric occlusion (Windsor et al., 2019). Our computational modeling corroborates the efficacy of this approach to diminish ribonucleolytic activity. As shown in Figures 2b and 3, AlphaFold2 predicts that a key active-site residue, His119, is dislocated significantly upon cyclization, which should deter catalysis of RNA cleavage (Figure S2). The linker also introduces significant steric bulk in the vicinity of the active site; Figure 2c suggests that even a substrate with just two nucleotides on the 3' side of the scissile phosphodiester bond clashes with the linker. Thus, conformational distortion and steric occlusion appear to work in tandem to achieve the >300-fold inactivation of ribonucleolytic activity and provide a $k_{\text{cat}}/K_{\text{M}}$ value that is comparable to that of other RNase 1 zymogens (Johnson et al., 2006; Plainkum et al., 2003; Windsor et al., 2019). Given that the thermostability of the zymogen returns nearly to that of wild-type RNase 1 upon cleavage (Figure 5b), we hypothesize that structural relaxation is responsible for the ability of the cleaved zymogen to achieve nearly wild-type ribonucleolytic activity and is a testament to the remarkable conformational stability of ribonucleases (Khan & James, 1998; Vilà et al., 2009). The newly unconstrained residues of the cleaved linker could partially occlude the active site and lead to a ribonucleolytic activity that is slightly less than that of wild-type RNase 1.

The activation of the zymogen is both expeditious and specific to the linker (Figure 5a,c), as desired for our context. 3CL^{Pro} cleaves a peptide bond following a glutamine residue (Koudelka et al., 2021). Although seven endogenous glutamine residues exist in our zymogen as possible off-target 3CL^{Pro} proteolysis sites, each is in a context that is incompatible with the substrate specificity of 3CL^{Pro} (Table S1). We believe that the high degree of topological complementarity between the zymogen and 3CL^{Pro} (Video S1), along with the relative flexibility of the zymogen linker and its ability to weave into the active site of 3CL^{Pro} (Figures 4 and S3), explain the appreciable rate of 3CL^{Pro} cleavage of the zymogen linker (which is $\sim 3\%$ that for cleaving the same eight-residue sequence in an untethered peptide).

Our coupled system (Figure 1) enables the detection of even low concentrations of 3CL^{PRO} within a timeframe comparable to RADT (Figure 6). It is estimated that an infected individual harbors up to 10^9 – 10^{11} SARS-CoV-2 virion particles in total and that patient samples contain $>10^6$ viral copies per mL, even during early infection (Pan et al., 2020; Puhach et al., 2023; Sender et al., 2021). Though the number of 3CL^{PRO} copies produced per virion has not been reported, we anticipate that the importance of 3CL^{PRO} to the SARS-CoV-2 replicase complex means that infected patient samples harbor zymogen-detectable concentrations of 3CL^{PRO}. In support of this hypothesis, immunofluorescence and immunoblotting assays have detected 3CL^{PRO} within infected cells as soon as 6 h post-infection (O'Brien et al., 2021; Shi et al., 2022). Although nanomolar concentrations of 3CL^{PRO} can be detected directly with an assay for proteolytic activity (e.g., with a fluorogenic peptide substrate), we recently reported that the detection of 25 nM 3CL^{PRO} requires high micromolar concentrations of the peptide substrate and assay times >30 min (Wralstad et al., 2023). By contrast, all reagents in our zymogen amplified assay are nanomolar or lower, and we easily detect 3CL^{PRO} within 15 min.

Critically, because the linker sequence in our zymogen is similar to endogenous 3CL^{PRO} polyprotein recognition sequences, we believe that our detection strategy is resistant to viral mutation-based sensitivity loss. In addition, 3CL^{PRO} is not under the same magnitude of selective pressure as other diagnostic targets, such as the spike and nucleocapsid proteins. These attributes are intrinsic advantages of a function-based diagnostic strategy and should mitigate the retooling that has been required of other SARS-CoV-2 diagnostics upon the emergence of variants (Alquraan et al., 2023; Ascoli, 2021).

3.1 | Conclusions

We have demonstrated that an engineered ribonuclease zymogen can be used for the sensitive detection of a viral protease. Our computational analyses and biophysical experiments support the hypothesis that conformational strain impairs ribonucleolytic activity in a manner that is reversible upon linker cleavage. The signal amplification that results from this coupled enzyme assay enables us to detect even low nanomolar concentrations of 3CL^{PRO} in a timeframe comparable to rapid antigen detection testing. Future efforts will focus on adapting this proof-of-concept to a point-of-care or at-home diagnostic tool, including immobilizing the zymogen for lateral flow assays, ensuring discrimination between the ribonucleolytic activity of the activated zymogen and patient-

derived ribonucleases, and developing alternative ribonuclease substrates that would enable facile detection of zymogen activation without fluorimetry.

4 | EXPERIMENTAL PROCEDURES

4.1 | Modeling the zymogen and its interactions

AlphaFold2 does not accept circular proteins as an input. Accordingly, the sequence of the circular zymogen was cleaved in four locations (Figure S1), and each of these sequences was submitted to AlphaFold2 for structural modeling (Mirdita et al., 2022). The suitability of each permutant model was evaluated based on its pLDDT scores and structural backbone alignment to the progenitor RNase 1 structure (PDB ID: 1z7x) (Johnson et al., 2007).

To model the steric clash between the zymogen and an RNA substrate, PyMOL was used to structurally align the zymogen models and the empirical RNase 1 structure to the structure of bovine RNase A that had been co-crystallized with a substrate analog, d(ApTpApApG) (PDB ID: 1rcn) (Fontecilla-Camps et al., 1994).

The ClusPro protein–protein docking server (Desta et al., 2020; Kozakov et al., 2013; Kozakov et al., 2017; Vajda et al., 2017) was used to predict the interactions of the Q37|R38 permutant with SARS-CoV 3CL^{PRO} (PDB ID: 1uj1) (Yang et al., 2003).

4.2 | Preparing the zymogen and protease

The 3CL^{PRO}-directed ribonuclease zymogen was prepared by methods similar to those described previously (Windsor et al., 2019). Briefly, Gibson assembly was used to construct an expression plasmid that combined five gene fragments 5' to 3' along the sense strand: (1) the *NpuC* fragment of the split intein from *Nostoc punctiforme* PCC73102, (2) residues 58–122 of mature *Homo sapiens* RNase 1, (3) residues ATLQSGNA to serve as a cyclizing linker for RNase 1 with recognition by 3CL^{PRO}, (4) residues 5–57 of RNase 1, and (5) the *NpuN* fragment of the split intein (Shah & Muir, 2014; Zettler et al., 2009).

Electrocompetent BL21(DE3) *E. coli* were transformed with the assembled plasmid and positive selection by using $200 \mu\text{g mL}^{-1}$ ampicillin. Cultures were grown to $\text{OD}_{600} = 1.80$ in Terrific Broth at 37°C with shaking at 250 RPM, and zymogen expression was induced by the addition of isopropyl β -D-

1-thiogalactopyranoside (to 1 mM) and growth for 4 h. Cultures were pelleted by centrifugation, and the pellets were stored at -70°C .

Pelleted *E. coli* cells were thawed and resuspended in 20 mM Tris-HCl buffer, pH 7.6, containing EDTA (10 mM) at room temperature. The cells were lysed by sonication with 15 rounds of 10-s sonication at 30% amplitude, followed by ≥ 60 s on ice. The lysate was subjected to centrifugation, and inclusion bodies were denatured in 20 mM Tris-HCl buffer, pH 8.0, containing guanidinium-HCl (7 M), EDTA (10 mM), and DTT (100 mM) at room temperature. The solubilized protein was diluted 10-fold with 20 mM acetic acid, and the resulting suspension was clarified by centrifugation. The supernatant was added dropwise to a refolding buffer of 100 mM Tris-HCl buffer, pH 7.8, containing EDTA (10 mM), L-arginine (0.5 M), reduced glutathione (1.0 mM), and oxidized glutathione (0.2 mM). The zymogen was allowed to fold at 4°C without agitation for 5 days. The folded zymogen was purified by gel-filtration and cation-exchange fast protein liquid chromatography. All chromatography buffers were treated with DEPC prior to use, except for Tris, which was added from ribonuclease-free stocks. Purified protein was buffer-exchanged into 50 mM sodium acetate buffer, pH 5.0, flash-frozen in liquid nitrogen, quantified by BCA assay, and stored at -70°C . Protein purity was verified by SDS-PAGE, and protein identity was confirmed by mass spectrometry (vide infra).

Authentic SARS-CoV-2 3CL^{PRO} was prepared as we reported recently (Wralstad et al., 2023).

4.3 | Monitoring the time course of zymogen activation by 3CL^{PRO}

Zymogen (25 μM) and 3CL^{PRO} (1 μM) were mixed in 50 mM HEPES-NaOH buffer, pH 7.5, and the resulting solution was incubated at 20°C without agitation. At each time point, an aliquot of the reaction mixture was acidified to $\sim 0.1\%$ v/v formic acid to halt proteolysis, as 3CL^{PRO} has negligible activity at pH < 5 (Huang et al., 2004; Solowiej et al., 2008). High-resolution mass spectrometry of an 8 pmol sample was performed with ESI mass spectrometry on an Agilent 6530C Accurate-Mass Q-TOF mass spectrometer equipped with a PLRP-S column (1000 Å, 5- μm , 50 mm \times 2.1 mm) from Agilent Technologies. A gradient of 5–95% v/v acetonitrile (0.1% v/v formic acid) in water (0.1% v/v formic acid) over 7 min was used for all samples. Before Q-TOF LC-MS analysis, all samples were passed through a Spin-X Centrifugal Tube Filter (0.22- μm , cellulose acetate membrane) from R&D Systems (Minneapolis, MN).

4.4 | Measuring the thermostability of the zymogen

Differential scanning fluorimetry (DSF) was used to determine the thermostability of the zymogen before and after activation. Zymogen was cleaved as in the time-course monitoring (vide supra), apart from using higher protein concentrations (94.1 μM zymogen, 3.76 μM 3CL^{PRO}) to achieve final concentrations amenable to DSF. After 1 h, SYPRO Orange protein gel stain (Supelco) was added to achieve 1 mg mL⁻¹ protein and 50 \times SYPRO Orange (vendor stock: 5000 \times in DMSO) in 50 mM HEPES-NaOH buffer, pH 7.5. Aliquots of the uncleaved zymogen, wild-type RNase 1, and 3CL^{PRO} were similarly prepared with SYPRO Orange. The resulting samples were heated from 15 to 95°C at $1^{\circ}\text{C}/\text{min}$ with a QuantStudio 7 Flex Real-Time PCR system (Applied Biosystems); fluorescence was monitored in real-time with $\lambda_{\text{ex}} = 470 \pm 15$ nm and $\lambda_{\text{em}} = 586 \pm 10$ nm. Data were processed with Protein Thermal Shift software (Applied Biosystems) using the Boltzmann fitting method. Values of T_{m} represent the temperature at which the fluorescence reached 50% of its maximum.

To characterize the potential for off-target proteolytic degradation, the zymogen was incubated with 3CL^{PRO} in 50 mM HEPES-NaOH buffer, pH 7.5, for 3 h (94.1 μM zymogen, 3.76 μM 3CL^{PRO}). Aliquots of cleaved and uncleaved zymogen were diluted to 0.4 mg mL⁻¹ with 50 mM HEPES-NaOH buffer, pH 7.5, mixed 1:1 with 2 \times Laemmli sample buffer (Bio-Rad) containing 2-mercaptoethanol (Sigma-Aldrich), incubated at 98°C for 5 min, cooled, and subjected to electrophoresis (2 μg load) at 4°C on a precast polyacrylamide/Tris-glycine SDS-PAGE gel (Bio-Rad) alongside a molecular weight standard (Thermo Fisher Scientific). The gel was stained with Bio-Safe Coomassie G-250 (Bio-Rad), destained in ultrapure water, and imaged with an Amersham 600 gel imager (Cytiva). Image editing with ImageJ software (Schroeder et al., 2021) consisted only of cropping and brightness/contrast adjustment to maximize band sensitivity.

4.5 | Assaying the ribonucleolytic activity of the zymogen

The tetranucleotide ribonuclease substrate 6-FAM-dAr_U(dA)₂-6-TAMRA was obtained from Microsynth AG and had a mass of 2307.5 Da (expected, 2312.7 Da) according to MALDI-TOF mass spectrometry (Figure S6). Catalysis of RNA hydrolysis was assessed by mixing the uncleaved zymogen (12.5 nM) with 6-FAM-dAr_U(dA)₂-6-TAMRA (0.20 μM) in ribonuclease-free 100 mM Tris-HCl buffer,

pH 7.5, containing NaCl (10 mM). Ultrapure water was DEPC-treated before the addition of Tris, due to the reactivity of its primary amino group with DEPC. Substrate fluorescence was measured at $\lambda_{\text{ex}} = 493 \pm 5$ nm and $\lambda_{\text{em}} = 515 \pm 5$ nm with a Spark multimode plate reader (Tecan) before the addition of zymogen to determine the background fluorescence, I_0 . After adding zymogen, the reaction mixture was incubated at 25°C and monitored continuously for 4 min. Wild-type RNase 1 was then added to a concentration of ~ 25 μM to cleave all of the substrate and determine I_{max} . The value of $k_{\text{cat}}/K_{\text{M}}$ was calculated with the equation:

$$\frac{k_{\text{cat}}}{K_{\text{M}}} = \frac{\Delta I/\Delta t}{(I_{\text{max}} - I_0)[E]} \quad (1)$$

where $\Delta I/\Delta t$ is the slope of the fluorescence versus time plot collected during the 4-min observation period, and $[E]$ is the concentration of enzyme.

Catalysis of RNA cleavage by the activated zymogen was determined by first treating the zymogen with 3CL^{pro} as in the DSF assay (vide supra). The ribonucleolytic activity of the cleaved zymogen was then assayed analogously to the uncleaved zymogen, except for the use of only 12.5 pM of the activated zymogen.

Real-time detection of 3CL^{pro} by zymogen cleavage and subsequent turn-on of ribonucleolytic activity was accomplished by mixing variable zymogen concentrations (5000, 500, or 50 pM) with variable 3CL^{pro} concentrations (1000, 500, 250, 100, 25, 10, 5, 1, or 0 nM) and 200 nM substrate as before, now with continuous monitoring for 15 min. All other reaction conditions were consistent with the assay of the intact and activated zymogen.

To evaluate the detection sensitivity for 3CL^{pro} with our amplified assay, we determined for each concentration of zymogen and 3CL^{pro} whether the following inequality was satisfied within the monitoring period:

$$I_{\text{P}} > I_{\text{B}} + 3(s_{\text{P}} + s_{\text{B}}) \quad (2)$$

where I_{P} is the mean fluorescence intensity of a 3CL^{pro}-containing reaction sample, I_{B} is the mean fluorescence intensity of a blank reaction sample containing zymogen but no 3CL^{pro}, s_{P} is the fluorescence intensity sample standard deviation of a 3CL^{pro}-containing reaction sample, and s_{B} is the fluorescence intensity sample standard deviation of a blank reaction sample (Long & Winefordner, 1983). The factor of 3 enforces a <0.13% chance that a signal from the 3CL^{pro}-containing sample results from a random signal fluctuation not related to zymogen linker cleavage. All statistics were calculated using the fluorescence intensity values of replicate reactions at each time point. 3CL^{pro}-containing samples that

satisfy Equation (2) are above the limit of detection with a >99.87% probability of not making either a type I error (i.e., erroneous confirmation of 3CL^{pro} presence, a “false positive”) or a type II error (i.e., failure to identify 3CL^{pro} presence, a “false negative”).

To determine the catalytic efficiency of zymogen linker cleavage by 3CL^{pro}, time-course data were fitted by nonlinear regression to eq. S14 of Supporting Information “Primer: Ribonucleolytic Activity of the Uncleaved and Cleaved Zymogen.” Nonlinear regression was restricted to datasets from 500 and 5000 pM zymogen with $[3\text{CL}^{\text{pro}}] \geq 100$ nM, where the curvature of the time-course data was sufficient to allow for convergence of the nonlinear regression algorithm.


AUTHOR CONTRIBUTIONS

Evans Wralstad: Investigation; writing – original draft; methodology; validation; visualization; writing – review and editing; data curation. **Ronald T. Raines:** Funding acquisition; writing – review and editing; project administration; supervision; resources.

ACKNOWLEDGMENTS

We are grateful to Professor Sangeeta N. Bhatia (MIT) for the ideation that led to this work. E.C.W. was supported by a Graduate Research Fellowship from the NSF. This work was supported by National Institutes of Health (Grant Numbers R01 CA073808 and R21 AI171663).

ORCID

Evans C. Wralstad  <https://orcid.org/0000-0002-2281-7594>

Ronald T. Raines  <https://orcid.org/0000-0001-7164-1719>

REFERENCES

- Adamson B, Sikka R, Wyllie AL, Premrurit P. Discordant SARS-CoV-2 PCR and rapid antigen test results when infectious: a December 2021 occupational case series. medRxiv. 2022.
- Alquraan L, Alzoubi KH, Rababa'h SY. Mutations of SARS-CoV-2 and their impact on disease diagnosis and severity. Inform Med Unlocked. 2023;39:101256.
- Ascoli CA. Could mutations of SARS-CoV-2 suppress diagnostic detection? Nat Biotechnol. 2021;39:274–5.
- Chen H, Wei P, Huang C, Tan L, Liu Y, Lai L. Only one protomer is active in the dimer of SARS 3C-like proteinase. J Biol Chem. 2006;281:13894–8.
- Chyan W, Raines RT. Enzyme-activated fluorogenic probes for live-cell and in vivo imaging. ACS Chem Biol. 2018;13:1810–23.
- de Michelena P, Torres I, Ramos-García Á, Gozalbes V, Ruiz N, Sanmartín A, et al. Real-life performance of a COVID-19 rapid antigen detection test targeting the SARS-CoV-2 nucleoprotein for diagnosis of COVID-19 due to the Omicron variant. J Infect. 2022;84:e64–6.

- Desta IT, Porter KA, Xia B, Kozakov D, Vajda S. Performance and its limits in rigid body protein–protein docking. *Structure*. 2020;28:1071–81.
- Durdagi S, Dağ Ç, Dogan B, Yigin M, Avsar T, Buyukdag C, et al. Near-physiological-temperature serial crystallography reveals conformations of SARS-CoV-2 main protease active site for improved drug repurposing. *Structure*. 2021;29:1382–96.
- Fontecilla-Camps JC, de Llorens R, le Du MH, Cuchillo CM. Crystal structure of ribonuclease A-d(ApTpApApG) complex. Direct evidence for extended substrate recognition. *J Biol Chem*. 1994;269:21526–31.
- Gandhi S, Klein J, Robertson AJ, Peña-Hernández MA, Lin MJ, Roychoudhury P, et al. De novo emergence of a remdesivir resistance mutation during treatment of persistent SARS-CoV-2 infection in an immunocompromised patient: a case report. *Nat Commun*. 2022;13:1–8.
- Grum-Tokars V, Ratia K, Begaye A, Baker SC, Mesecar AD. Evaluating the 3C-like protease activity of SARS-coronavirus: recommendations for standardized assays for drug discovery. *Virus Res*. 2008;133:63–73.
- Huang C, Wei P, Fan K, Liu Y, Lai L. 3C-like proteinase from SARS coronavirus catalyzes substrate hydrolysis by a general base mechanism. *Biochemistry*. 2004;43:4568–74.
- Ippoliti C, De Maio F, Santarelli G, Marchetti S, Vella A, Santangelo R, et al. Rapid detection of the Omicron (B.1.1.529) SARS-CoV-2 variant using a COVID-19 diagnostic PCR assay. *Microbiol Spectrum*. 2022;10:e0099022–e.
- Isabel S, Abdulnoor M, Boissinot K, Isabel MR, de Borja R, Zuzarte PC, et al. Emergence of a mutation in the nucleocapsid gene of SARS-CoV-2 interferes with PCR detection in Canada. *Sci Rep*. 2022;12:10867.
- Johnson RJ, Lin SR, Raines RT. A ribonuclease zymogen activated by the NS3 protease of the hepatitis C virus. *FEBS J*. 2006;273:5457–65.
- Johnson RJ, McCoy JG, Bingman CA, Phillips GN Jr, Raines RT. Inhibition of human pancreatic ribonuclease by the human ribonuclease inhibitor protein. *J Mol Biol*. 2007;368:434–49.
- Kelemen BR, Klink TA, Behlke MA, Eubanks SR, Leland PA, Raines RT. Hypersensitive substrate for ribonucleases. *Nucleic Acids Res*. 1999;27:3696–701.
- Khan AR, James MNG. Molecular mechanisms for the conversion of zymogens to active proteolytic enzymes. *Protein Sci*. 1998;7:815–36.
- Koudelka T, Boger J, Henkel A, Schönherr R, Krantz S, Fuchs S, et al. N-Terminomics for the identification of in vitro substrates and cleavage site specificity of the SARS-CoV-2 main protease. *Proteomics*. 2021;21:e2000246–e.
- Kozakov D, Beglov D, Bohnuud T, Mottarella SE, Xia B, Hall DR, et al. How good is automated protein docking? *Proteins*. 2013;81:2159–66.
- Kozakov D, Hall DR, Xia B, Porter KA, Padhorny D, Yueh C, et al. The ClusPro web server for protein–protein docking. *Nat Protoc*. 2017;12:255–78.
- Long GL, Winefordner JD. Limit of detection: a closer look at the IUPAC definition. *Anal Chem*. 1983;55:713A–724A.
- Mahmoudinobar F, Britton D, Montclare JK. Protein-based lateral flow assays for COVID-19 detection. *Protein Eng Des Sel*. 2021;34:1–10.
- Mirdita M, Schütze K, Moriwaki Y, Heo L, Ovchinnikov S, Steinegger M. ColabFold: making protein folding accessible to all. *Nat Methods*. 2022;19:679–82.
- O'Brien A, Chen D-Y, Hackbart M, Close BJ, O'Brien TE, Saeed M, et al. Detecting SARS-CoV-2 3CLpro expression and activity using a polyclonal antiserum and a luciferase-based biosensor. *Virology*. 2021;556:73–8.
- Pan Y, Zhang D, Yang P, Poon LLM, Wang Q. Viral load of SARS-CoV-2 in clinical samples. *Lancet Infect Dis*. 2020;20:411–2.
- Park C, Kelemen BR, Klink TA, Sweeney RY, Behlke MA, Eubanks SR, et al. Fast, facile, hypersensitive assays for ribonucleolytic activity. *Methods Enzymol*. 2001;341:81–94.
- Plainkum P, Fuchs SM, Wiyakrutta S, Raines RT. Creation of a zymogen. *Nat Struct Biol*. 2003;10:115–9.
- Planas D, Saunders N, Maes P, Guivel-Benhassine F, Planchais C, Buchrieser J, et al. Considerable escape of SARS-CoV-2 Omicron to antibody neutralization. *Nature*. 2022;602:671–5.
- Puhach O, Meyer B, Eckerle I. SARS-CoV-2 viral load and shedding kinetics. *Nat Rev Microbiol*. 2023;21:147–61.
- Raines RT. Ribonuclease A. *Chem Rev*. 1998;98:1045–65.
- Ramos-Guzmán CA, Ruiz-Pernía JJ, Tuñón I. Unraveling the SARS-CoV-2 main protease mechanism using multiscale methods. *ACS Catal*. 2020;10:12544–54.
- Robles-Escajeda E, Mohl JE, Contreras L, Betancourt AP, Mancera BM, Kirken RA, et al. Rapid shift from SARS-CoV-2 Delta to Omicron sub-variants within a dynamic Southern U.S. borderplex. *Viruses*. 2023;15:658.
- Rockett R, Basile K, Maddocks S, Fong W, Agius JE, Johnson-Mackinnon J, et al. Resistance mutations in SARS-CoV-2 Delta variant after sotrovimab use. *N Engl J Med*. 2022;386:1477–9.
- Schroeder AB, Dobson ETA, Rueden CT, Tomancak P, Jug F, Eliceiri KW. The ImageJ ecosystem: open-source software for image visualization, processing, and analysis. *Protein Sci*. 2021;30:234–49.
- Sender R, Bar-On YM, Gleizer S, Bernshtein B, Flamholz A, Phillips R, et al. The total number and mass of SARS-CoV-2 virions. *Proc Natl Acad Sci U S A*. 2021;118:e2024815118.
- Service RF. Bad news for Paxlovid? Resistance may be coming. *Science*. 2022;377:138–9.
- Shah NH, Muir TW. Inteins: nature's gift to protein chemists. *Chem Sci*. 2014;5:446–61.
- Shi F-S, Yu Y, Li Y-L, Cui L, Zhao Z, Wang M, et al. Expression profile and localization of SARS-CoV-2 nonstructural replicase proteins in infected cells. *Microbiol Spectrum*. 2022;10:e0074422.
- Singh H, Tiwari K, Tiwari R, Pramanik SK, Das A. Small molecule as fluorescent probes for monitoring intracellular enzymatic transformations. *Chem Rev*. 2019;119:11718–60.
- Solowiej J, Thomson JA, Ryan K, Luo C, He M, Lou J, et al. Steady-state and pre-steady-state kinetic evaluation of severe acute respiratory syndrome coronavirus (SARS-CoV) 3CL^{PRO} cysteine protease: development of an ion-pair model for catalysis. *Biochemistry*. 2008;47:2617–30.
- Turcotte RF, Raines RT. Design and characterization of an HIV-specific ribonuclease zymogen. *AIDS Res Hum Retroviruses*. 2008;24:1357–63.
- Vajda S, Yueh C, Beglov D, Bohnuud T, Mottarella SE, Xia B, et al. New additions to the ClusPro server motivated by CAPRI. *Proteins*. 2017;85:435–44.
- Vilà R, Benito A, Ribó M, Vilanova M. Mapping the stability clusters in bovine pancreatic ribonuclease a. *Biopolymers*. 2009;91:1038–47.

- Windsor IW, Graff CJ, Raines RT. Circular zymogens of human ribonuclease 1. *Protein Sci.* 2019;28:1713–9.
- Wralstad EC, Sayers J, Raines RT. Bayesian inference elucidates the catalytic competency of the SARS-CoV-2 main protease 3CL^{pro}. *Anal Chem.* 2023;95:14981–9.
- Wu X, Wang R, Kwon N, Ma H, Yoon J. Activatable fluorescent probes for in situ imaging of enzymes. *Chem Soc Rev.* 2022;51:450–63.
- Yang H, Yang M, Ding Y, Liu Y, Lou Z, Zhou Z, et al. The crystal structures of severe acute respiratory syndrome virus main protease and its complex with an inhibitor. *Proc Natl Acad Sci U S A.* 2003;100:13190–5.
- Yuan Y, Jiao B, Qu L, Yang D, Liu R. The development of COVID-19 treatment. *Front Immunol.* 2023;14:1125246.
- Zettler J, Schütz V, Mootz HD. The naturally split *Npu* DnaE intein exhibits an extraordinarily high rate in the protein *trans*-splicing reaction. *FEBS Lett.* 2009;583:909–14.

SUPPORTING INFORMATION

Additional supporting information can be found online in the Supporting Information section at the end of this article.

How to cite this article: Wralstad EC, Raines RT. Sensitive detection of SARS-CoV-2 main protease 3CL^{pro} with an engineered ribonuclease zymogen. *Protein Science.* 2024;33(4):e4916. <https://doi.org/10.1002/pro.4916>